Electrostatic Interactions Between the Bni1p Formin FH2 Domain and Actin Influence Actin Filament Nucleation

Joseph L. Baker,[1,6] Naomi Courtemanche,[2,6] Daniel L. Parton,[5,6] Martin McCullagh,[1] Thomas D. Pollard,[2,3,4] and Gregory A. Voth[1,*]

1. Department of Chemistry, Institute for Biophysical Dynamics, James Franck Institute, and Computation Institute, The University of Chicago, 5735 S Ellis Ave., Chicago, IL 60637

2. Department of Molecular, Cellular and Developmental Biology, Yale University, P.O. Box 208103, New Haven, CT 06520-8103

3. Department of Molecular Biophysics and Biochemistry, Yale University, P.O. Box 208103, New Haven, CT 06520-8103

4. Department of Cell Biology, Yale University, P.O. Box 208103, New Haven, CT 06520-8103

5. Memorial Sloan-Kettering Cancer Center, 1275 York Avenue, New York, NY 10065

6. These authors contributed equally.

*Corresponding author email: gavoth@uchicago.edu

Running title: Formin/actin interactions influence actin filament nucleation

Supplemental Data

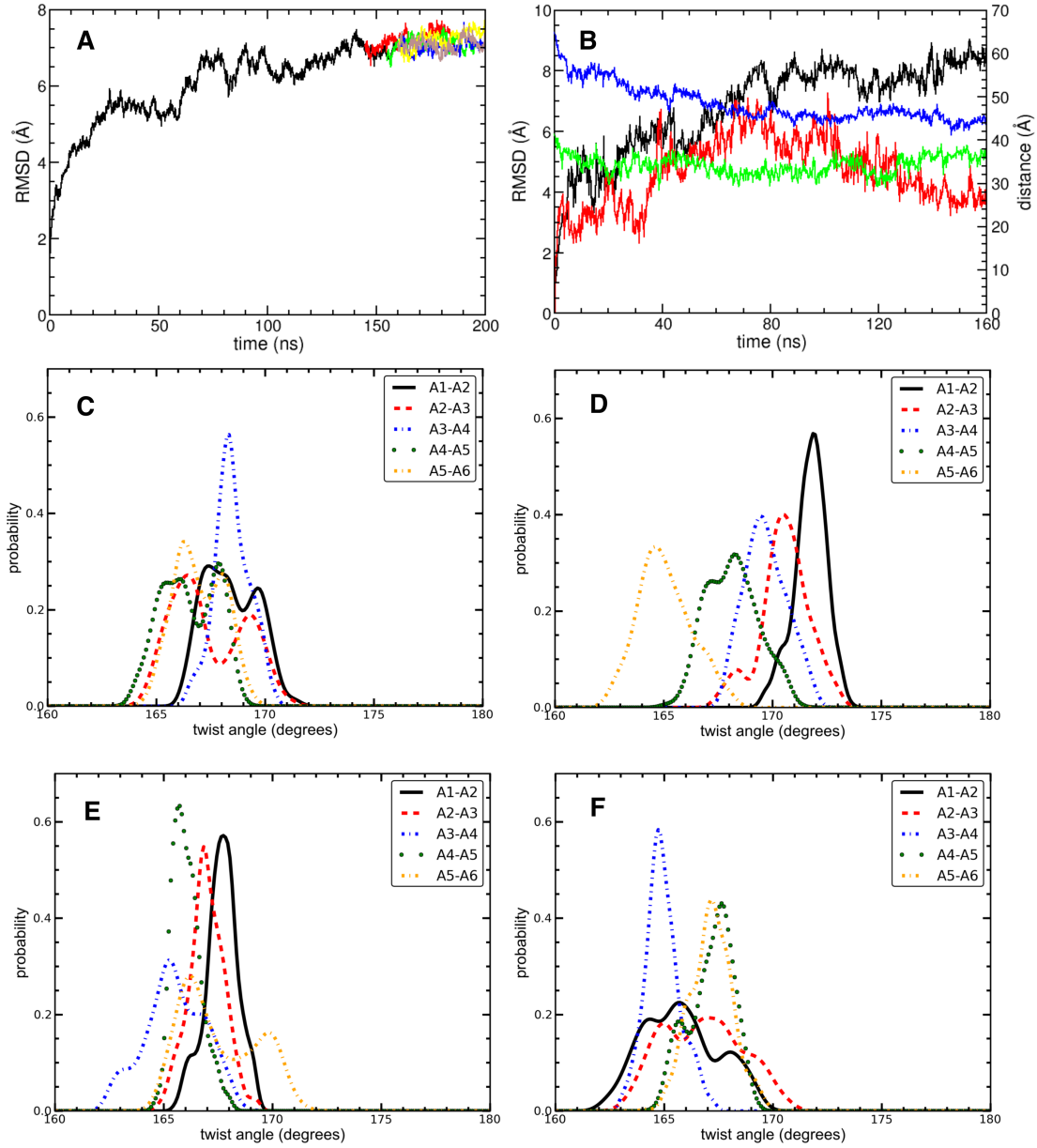

Figure S1. Changes in distances and angles in all-atom simulations related to Figure 1. (A) RMSD of the alpha carbons of the Bni1p/actin 7-mer system: (black) WT, (red) WTa, (green) WTb, (blue) R1423N, (yellow) K1467L, and (brown) R1423N/K1467L. The WTa, WTb and three mutant simulations are plotted starting where they were initiated along the WT simulation. (B) RMSD of the alpha carbons of the linker residues (1394-1415) for (black) FH2L and (red) FH2T, and the distance between the alpha-carbon atoms of A1393 and Q1416 at either end of the formin linker for (blue) FHTL and (green) FH2T. **(**C-F**)** Distributions of actin twist angles (angles of rotation around the filament axis to generate the next actin subunit toward the pointed end in the filament) during 160 ns simulations. A1-A2 is the barbed end twist. (C-B) Combined data from the WT, WTa and WTb simulations with distributions measured over the (C) first 20 ns and (D) last 20 ns of simulation. (E-F) Simulation of an Oda filament 30-mer without formin with distributions measured over the (E) first 20 ns and (F) last 20 ns of the simulation.

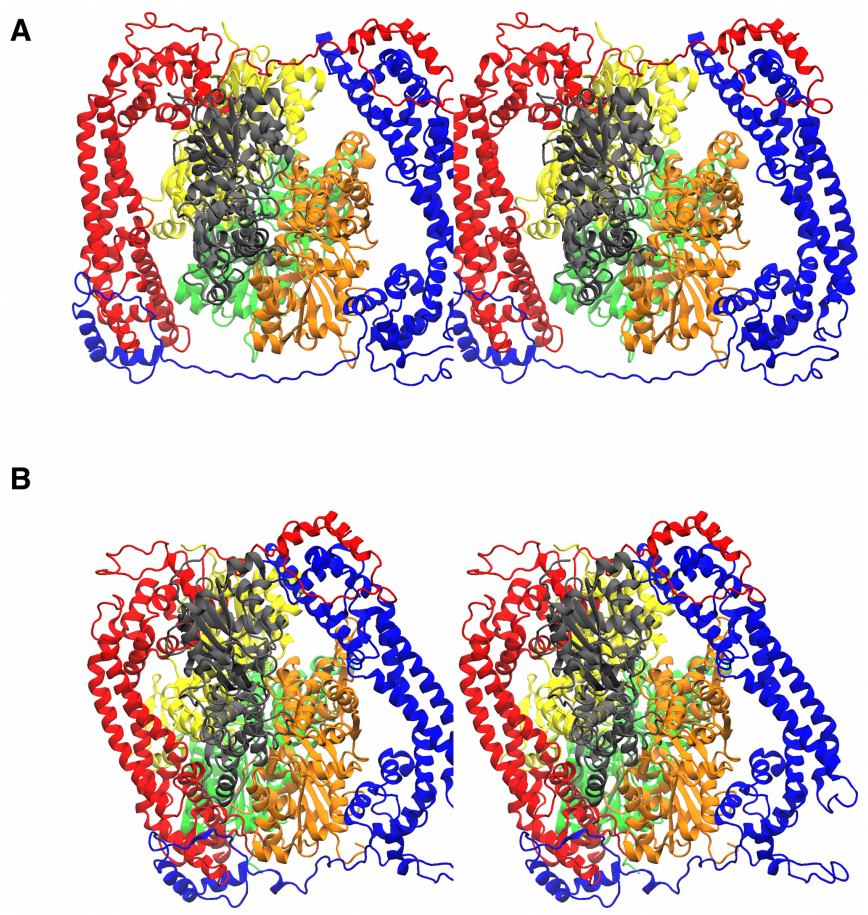

Figure S2. Stereo images of Figure 1B and 1C, related to Figure 1. Side-by-side stereo images showing the same perspectives of the formin dimer on actin as in (A) Figure 1B and (B) Figure 1C.

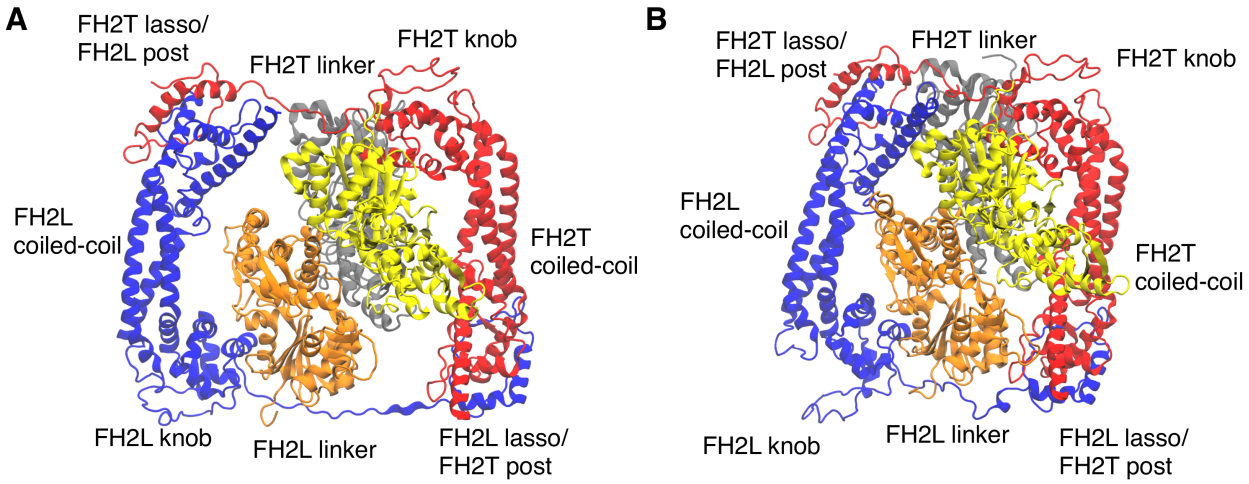

Figure S3. Comparison of the initial model and the refined model from all atom molecular dynamics simulation of a dimer of Bni1p FH2 domains associated with the barbed end of an actin filament as viewed from the actin filament pointed end, related to Figure 1. The same color scheme as Figure 1 is used. FH2L (blue), FH2T (red), and three actin monomers (A1, A2, and A3 in grey, orange, and yellow, respectively) are shown. The view is looking down the filament central axis from the pointed end, where actin monomers A4 through A7 have been removed for clarity. This figure provides a complementary view to the view in Figure 1 which looks down the filament axis from the barbed end of the actin filament.

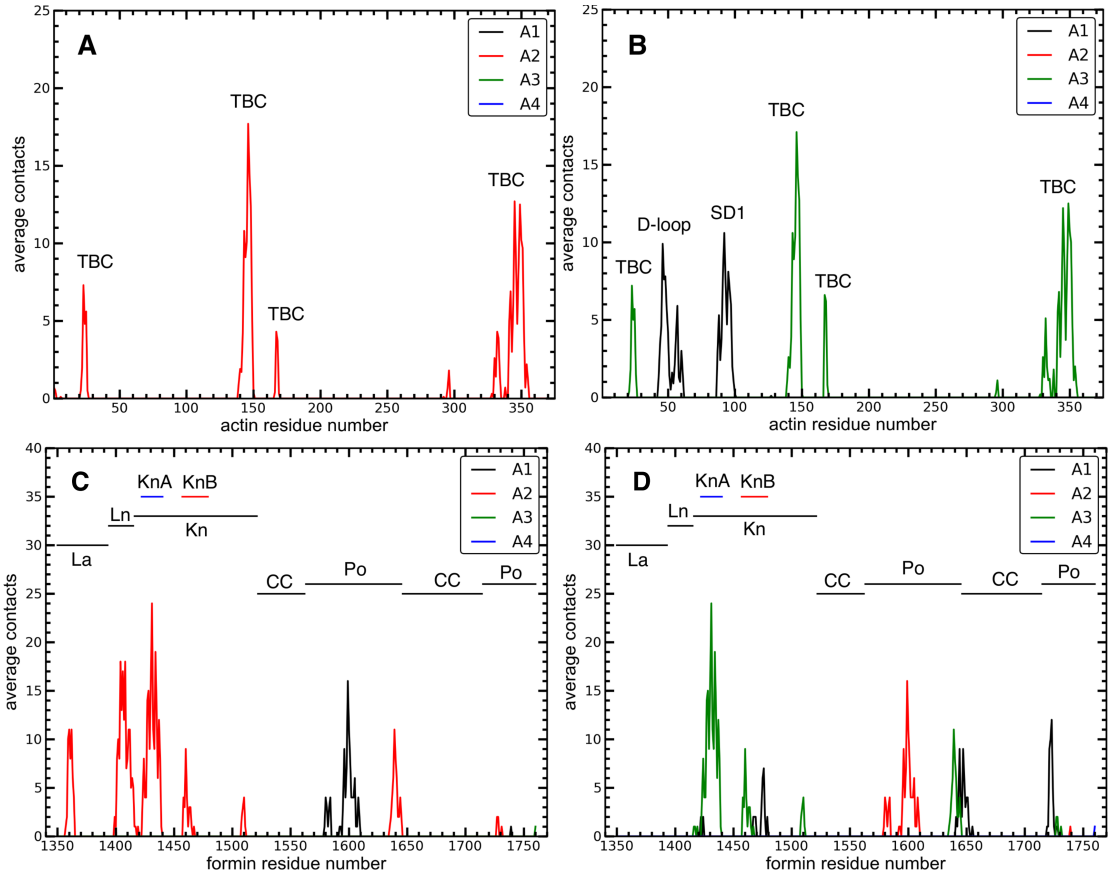

Figure S4. Plots of intermolecular contacts from simulations of the WT FH2 dimer with the actin heptamer, related to Figure 2. (A, B) Average number of contacts of the four terminal actin subunits (color code in the inset) and in the KnA and KnB helices of WT Bni1p. (A) Leading FH2 domain and (B) trailing FH2 domain. Labels are for the actin target-binding cleft (TBC), the actin D-loop, and a sub-region in subdomain 1 (SD1) of actin monomer A1. (C, D) Average number of contacts from a single static snapshot of the FH2 domains with actin subunits in a 7-mer in the 180 degree orientation from the Otomo crystal structure. (C) FH2L and (D) FH2T. Actin residues 1-3, 40-51 and 373-375 are missing in the Otomo crystal structure and they were not included in this calculation.

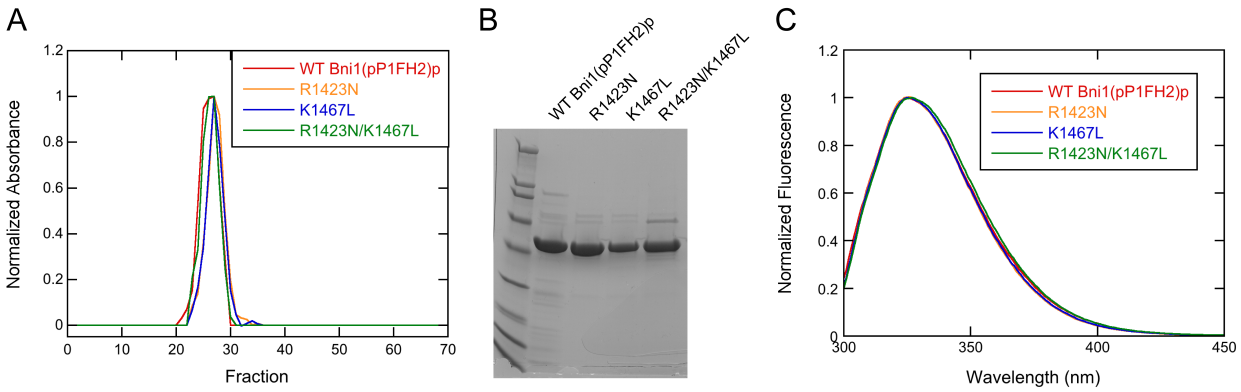

Figure S5. Solution characterization of Bni1p mutants, related to Figures 7 and 8. Conditions: 50 mM KCl, 1 mM $MgCl_2$, 1 mM EGTA, 10 mM imidazole (pH 7.0), 1 mM DTT. (A) Elution profiles of wild-type and mutant Bni1(pP1FH2)p following gel filtration on a 110 x 1.5 cm column of Sephacryl S-200 resin. (B) Coomassie-stained SDS-PAGE gel of purified wild-type and mutant Bni1(pP1FH2)p proteins. (C) Fluorescence emission spectra of 5 µM wild-type and mutant Bni1(pP1FH2)p proteins with excitation at 280 nm.

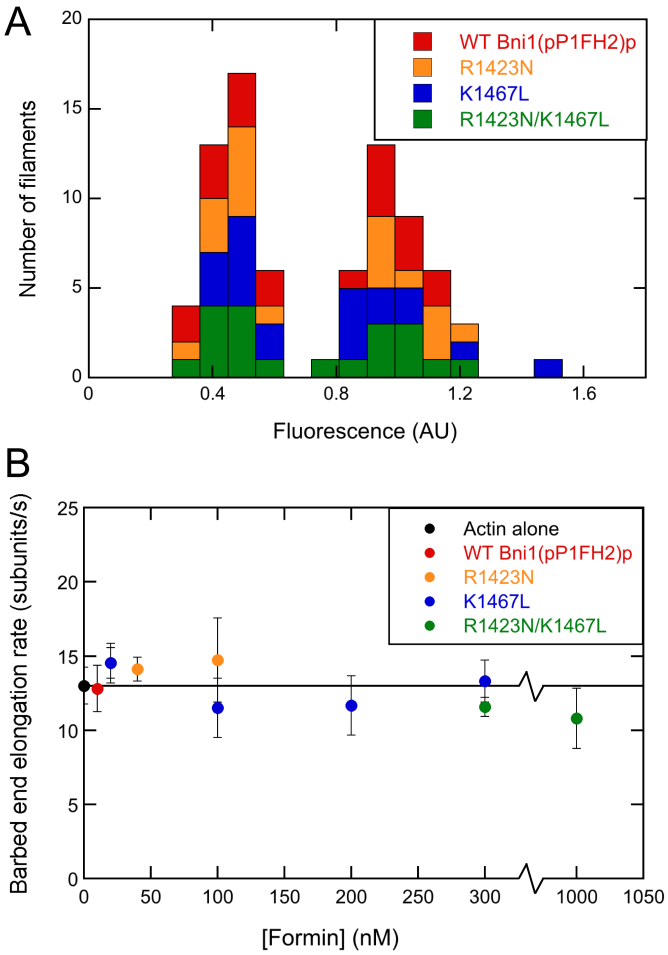

Supplemental Figure S6. Bni1(pP1FH2)p mutants preferentially incorporate unlabeled actin into filaments in the presence of profilin, and do not sequester monomers, related to Figures 7 and 8. Conditions: 1.5 mm actin (33% Oregon green-labeled) in 10 mM imidazole (pH 7.0), 50 mM KCl, 1 mM $MgCl_2$, 1 mM EGTA, 50 mM DTT, 0.3 mM ATP, 0.02 mM $CaCl_2$, 15 mM glucose, 0.02 mg/ml catalase, 0.1 mg/ml glucose oxidase and 0.5% methylcellulose (4,000 cP at 2% (w/v)). Data were collected with TIRFM. (A) Histogram of fluorescence intensities of filaments formed in the presence of 5 µM profilin and wild-type or mutant Bni1(pP1FH2). For each formin construct, the average fluorescence intensity along the entire length of 20 filaments was analyzed and normalized to the average of the peak with the larger signal. (B) Dependence of the elongation rate of free (not formin-bound) barbed ends on the concentration of wild-type or mutant Bni1(pP1FH2)p. Error bars are standard deviations of the mean elongation rate of at least 10 filaments.

Table S1. Definitions of features of Bni1p and actin, related to Figures 1 and 2.

Residues comprising feature	Feature name	Label
Bni1p		
1350-1393	Lasso	La
1394-1415	Linker	Ln
1416-1521	Knob	Kn
1422-1440	Knob Helix A	KnA
1457-1479	Knob Helix B	KnB
1522-1562,1646-1714	Coiled-coil	CC
1563-1645,1715-1760	Post	Po
Actin		
22-26, 139-149, 167-169, 338-355	Target-binding cleft	TBC

Table S2. Buried surface area on Bni1p FH2 domains and actin monomers A1 to A3, related to Figure 1

	Buried surface areas (Å^2)[a]		
Protein	**Initial**	**Final**	**Difference**
FH2L buried by A1	2.1 +/- 7.5	270 +/- 20	+268
FH2L buried by A2	910 +/- 130	1660 +/- 70	+750
FH2L buried by A3	59 +/- 40	105 +/- 30	+46
FH2T buried by A1	570 +/- 100	1110 +/- 70	+540
FH2T buried by A2	2.2 +/- 7.5	424 +/- 40	+422
FH2T buried by A3	690 +/- 110	1170 +/- 80	+480
A1 buried by FH2L	2.2 +/- 8.3	250 +/- 30	+248
A2 buried by FH2L	890 +/- 130	1630 +/- 70	+740
A3 buried by FH2L	56 +/- 34	102 +/- 30	+46
A1 buried by FH2T	580 +/- 90	1020 +/- 60	+440
A2 buried by FH2T	2.2 +/- 7.6	380 +/- 40	+378
A3 buried by FH2T	690 +/- 110	1170 +/-100	+480

[a]Buried surface is calculated as $SASA_{X,free} - SASA_{X,buried\ by\ Y}$, where X and Y represent protein components, free means that the calculation of the SASA is performed for the free protein, and buried by Y means that the calculation of the SASA is performed in the presence of protein component Y. The initial and final values are averaged over the first and last 10 ns of the WT simulation respectively. SASA values were calculated with VMD (Humphrey et al., 1996, main article reference).

Table S3. Solvent accessible surface area of Bni1p domains and actin TBC, related to Figure 1

	Solvent accessible surface areas (Å^2)[a]		
Protein domains	**Initial**	**Final**	**Difference**
FH2L Lasso	3160 +/- 60	2900 +/- 110	-260
FH2L Linker	2320 +/- 90	1700 +/- 72	-620
FH2L Knob	6040 +/- 120	6180 +/- 240	+140
FH2L helix KnA[b]	*980 +/- 70*	*770 +/- 40*	*-210*
FH2L helix KnB[b]	*1480 +/- 40*	*1470 +/- 40*	*-10*
FH2L CC	6030 +/- 110	6220 +/- 130	+190
FH2L Post	6420 +/- 170	6130 +/- 140	-290
FH2T Lasso	3170 +/- 80	3160 +/- 70	-10
FH2T Linker	2120 +/- 110	1680 +/- 90	-440
FH2T Knob	5633 +/- 90	5390 +/- 120	+240
FH2T helix KnA	*870 +/- 50*	*710 +/- 50*	*-160*
FH2T helix KnB	*1170 +/- 80*	*1000 +/- 40*	*-170*
FH2T CC	6100 +/- 140	6190 +/- 170	+90
FH2T Post	6370 +/- 50	5630 +/- 120	-740
Actin A2 TBC	850 +/- 70	720 +/- 30	-130
Actin A3 TBC	660 +/- 50	400 +/- 40	-260

[a]SASA values are calculated for each feature assuming that all other protein components of the system can contribute to reducing the SASA. The initial and final values are averages over the first and last 10 ns of the WT simulation, respectively. SASA values were calculated with VMD (Humphrey et al., 1996, main article reference).

[b]Italicized rows indicate that these are subdomains of the formin knob.

Table S4. Total interaction energies in kcal/mol between individual FH2 knob helices and actin TBC, related to Table 2.

Interaction	*WT*	*R1423N*	*K1467L*	*R1423N/K1467L*
Subunit A2 with				
FH2L-KnA	-40.1	-16.5	-16.1	+0.1
FH2L-KnB	-65.6	-29.3	-35.4	-15.5
Subunit A3 with				
FH2T-KnA	-37.1	+0.5	-28.5	-8.1
FH2T-KnB	-80.5	-77.6	-5.6	-0.8

Table S5. Evolutionary conservation of residues R1423 and K1467, related to Figure 3.

Formin name	Organism	Residues 1420-1425[a]	Residues 1465-1470[a]
Bni1p	*S. cerevisiae*	FLS**R**DI	LS**K**SEI
Bnr1p	*S. cerevisiae*	FLS**R**DL	FC**K**EEL
Cdc12p	*S. pombe*	YMSESL	LSSDKV
For3p	*S. pombe*	FMPVDL	ND**RK**FF
Fus1p	*S. pombe*	LLPDTV	D**R**ASLA
Dia1	*H. sapiens*	VLDS**K**T	I**K**QMPE
Dia2	*H. sapiens*	ILDP**K**T	V**K**HLPE
Dia3	*H. sapiens*	FLDP**K**I	I**K**HLPD
FHOD1	*H. sapiens*	VLDP**K**R	LTMMPT
FHOD3	*H. sapiens*	VLDS**K**R	LTMIPT
Daam1	*H. sapiens*	VIDG**R**R	LL**K**FVP
FMN1	*H. sapiens*	LLDG**K**R	YEN**R**AQ
INF2	*H. sapiens*	FLDA**K**K	L**K**LLPE
Delphilin	*H. sapiens*	ILSH**K**K	LLFAPD
Diaphanous	*D. melanogaster*	VLDS**K**T	IQYLPP
Cappuccino	*D. melanogaster*	VLDPER	SNIQAT
CYK-1	*C. elegans*	VIHDDK	L**R**SAMP
dDia1	*D. discoideum*	VIDP**K**K	LEQYLP
dDia2	*D. discoideum*	VIDM**K**K	LLQFAP

[a]Sequences were aligned using ClustalW (Goujon et al., 2010; Larkin et al., 2007) and the residues at positions that correspond to residues 1420-1425 and 1465-1470 in Bni1p are listed. Positively charged residues at positions 1422, 1423, 1466, 1467 and 1468 are highlighted in red.

Supplemental Experimental Procedures

Additional Details On The Modeling and All-Atom Simulation of the Formin/Actin System

The modeling proceeded in three main stages. Firstly, two copies of the FH2-actin co-crystal structure were aligned against the actin filament structure, aiming to preserve the interactions between the knob subdomains and the TBC regions of actins 2 and 3. Due to the 167° filament twist, this initial alignment left the two FH2 subunits unconnected. To reconnect the subunits, the lasso subdomains were realigned independently, aiming to recapitulate the lasso-post binding mode observed in the FH2-actin co-crystal. In the final stage, the linker regions between the lasso subdomains and the rest of the FH2 structure were remodeled as unstructured chain, using the Modeller software package (Sali and Blundell, 1993). In the resultant formin/actin structure, the FH2 knob and actin TBC regions were in close contact (as observed in the FH2-actin co-crystal), while the post/lasso regions were not initially in contact with the filament, due to the 167° twist conformation.

The system was solvated such that there was at least 15 Å of padding in each direction so that the protein did not see its periodic image during the course of the simulation. The N-terminus of the actin monomers was acetylated, and all other residues in the system were modeled in their standard states of protonation at a pH value of 7. The system was neutralized with 0.18 M KCl. The Solvate and Autoionize plugins in the VMD software package (Humphrey et al., 1996, main article reference) were used to solvate and add counter-ions to the system. The WT system consisted of a total of 637,699 atoms.

To prepare the Bni1p/actin wild-type (WT) system for simulations, we carried out an energy minimization using NAMD (Phillips, et al., 2005, main article reference) in which the restraints on the WT system were gradually released. A heating phase was carried out with

restraints on the backbone atoms of the protein, ADP, the Mg^{2+} ion and coordinating waters. This heating phase was carried out over 200 ps, and we raised the temperature gradually to 310 K. Following the heating phase, a restrained equilibration was performed with restraints on the protein backbone, ADP, the Mg^{2+} ion and coordinating waters. The restraints during equilibration were gradually reduced from 10 kcal/mol/Å^2 to 0.1 kcal/mol/Å^2 over the course of 400 ps. This was followed by unrestrained dynamics.

The waters and ions within 5 Å of the protein were also kept from the WT snapshot. To these systems we then added back additional waters and ions to fully solvate and neutralize the system using the Solvate and Autoionize plugins from VMD (Humphrey et al., 1996, main article reference). The R1423N, K1467L, and R1423N/K1467L systems consisted of a total of 640,191 atoms, 640,196 atoms, and 640,181 atoms, respectively. For the mutant simulations, we carried out 200 ps of restrained heating, as described above, and then followed this by a 400 ps restrained equilibration phase also as described for the WT simulations. Finally, we carried out 50 ns of unrestrained dynamics for each of the three mutant systems.

For the simulation of the Oda actin 30-mer filament, we generated a filament of 30 actin subunits without formin. The filament long axis pointed along the z-direction. In the x and y directions we used 8 Å of water padding as in previous simulations of the filament (Saunders and Voth, 2011, main article reference), and in the z direction we used 15 Å of padding. Neutralization of the system was carried out with 0.180 M KCl. The N-terminus of the actin monomers was acetylated, and all other residues in the system were modeled in their standard states of protonation at a pH value of 7. The system was energy minimized, followed by heating over 100 ps to 310 K and equilibration over 200 ps during which restraints on the protein

backbone, ADP, Mg^{2+}, and its coordinating waters were gradually reduced. The production simulation was carried out for approximately 160 ns.

Dynamics in all all-atom simulations were run with a 2 fs integration timestep. In order to accommodate a 2 fs timestep, the hydrogen bonds in all systems were restrained. The unrestrained production runs were carried out using the NPT ensemble, and the system pressure was kept at 1 atm using the Langevin piston method implemented in NAMD (Phillips, et al., 2005, main article reference). The Langevin piston period and Langevin piston decay time was set to 200 fs (2 ps) and 100 fs (2 ps) for the formin simulations (Oda 30-mer simulations), respectively. The system temperature was kept at 310 K using a Langevin thermostat, and the damping coefficient for the thermostat was set to a value of 5 ps^{-1}.

Additional Details On The Bni1p/Actin Coarse-Grained (CG) Model

We built the CG models of Bni1p and actin using the all-atom Bni1p data from the actin 7-mer simulations performed for this paper and actin data from previous simulations of ADP bound actin 13-mer filament (Saunders and Voth, 2011, main article reference). The excluded volume interactions were taken to be the repulsive part of a Lennard-Jones 6-12 potential with the sigma parameter given by the radius of gyration of each residue averaged over the all-atom simulation. The hENM bond distances and force constants were fit to the all-atom fluctuations as described previously (Lyman et al., 2008, main article reference).

Charges were fit to each CG site in a least squares procedure to best fit the all-atom electrostatic potential. Data for charge fitting was taken from all-atom simulations (50 ns for actin and 20 ns for Bni1p). Charges for the CG wild-type Bni1p were fit from the WT simulation all-atom data, and the CG mutant formin charges were fit using the R1423N/K1467L all-atom data, due to the fact that we observed the largest effect on the electrostatic interaction energy for

both knob sites KnA and KnB with actin for that mutant. Symmetry was enforced by averaging over all monomers in both the Bni1p and the actin systems (two for Bni1p dimer and 13 for the actin filament). To account for charge screening, a parameter sweep was carried out for the dielectric constant and the Debye screening length with a CG actin filament composed of 26 actin monomers. The dielectric constant was scanned from 1.0 to 4.0 in intervals of 1.0 and Debye screening length from 0.0 Å to 0.5 Å in intervals of 0.05 Å. A dielectric of 1.0 and a Debye screening length of 0.25 Å gave the best agreement of the twist, rise and torsional stiffness of the actin filament as compared to experimental and all-atom simulation values (Fan et al., 2012). Therefore, a Debye screening length of 0.25 Å and a dielectric of 1.0 were chosen from the parameter search and used for all subsequent simulations. The electrostatic interactions were cutoff at 30.0 Å. Simulations were run for at least 10^7 time steps with an integration timestep of 10 fs. The CG dimer system consists of 1574 total CG sites, and the CG heptamer system consists of 3454 CG sites.

Protein Purification

All formin constructs were expressed in BL21 DE3 RP CodonPlus cells (Stratagene). Cells were resuspended in 500 mM NaCl, 50 mM Tris (pH 8.0), 1 mM DTT, and lysed by sonication. Following clarification by centrifugation at 21,200 g for 45 min, the lysate supernatant was incubated with glutathione Sepharose resin for 1 h with rotation at 4 ºC. The supernatant and resin were then poured into an empty column, washed with lysis buffer, eluted with 100 mM glutathione in lysis buffer, concentrated to a volume of ~2 mL using a centrifuge filter device (30 kDa MWCO, Millipore) and dialyzed into 100 mM NaCl, 50 mM Tris (pH 8.0), 1 mM DTT. The GST tag was cleaved by incubating with 1 mM TEV protease overnight at 4 ºC, and separated

from the formin by gel filtration on S-200 resin. All formin constructs were dialyzed into 50 mM KCl, 10 mM imidazole (pH 7.0), 1 mM $MgCl_2$, 1 mM EGTA and flash-frozen.

Muscle actin was purified from an acetone powder of chicken skeletal muscle (Trader Joe's) using one cycle of polymerization and depolymerization followed by gel filtration and storage in Ca-Buffer-G (2 mM Tris-HCl, pH 8.0, 2 mM ATP, 0.1 mM $CaCl_2$, 1 mM NaN_3, 0.5 mM DTT) (MacLean-Fletcher and Pollard, 1980). Actin was labeled on cysteine 374 with either Oregon Green 488 iodoacetamide or pyrenyl iodoacetamide (Invitrogen). Labeled and unlabeled actin was stored at 4 ºC. We used extinction coefficients of 26,000 $M^{-1} cm^{-1}$ at $\lambda = 290$ nm for unlabeled actin, 78,000 $M^{-1} cm^{-1}$ at $\lambda = 491$ nm for Oregon Green, and 45,500 $M^{-1}cm^{-1}$ at $\lambda = 344$ nm for pyrene.

S. cerevisiae profilin was expressed in *E. coli* BL21 DE3 cells from plasmid pMW172 and purified by affinity chromatography on poly-L-proline coupled to Sepharose 4 Fast Flow (17-0981-01, Amersham Pharmacia, Piscataway, NJ) (Kaiser et al., 1989; Lu and Pollard, 2001). Purified profilin was dialyzed into KMEI and stored long-term at 4 ºC. Before experiments were performed, profilin was centrifuged at high speed (128,000 x g, 30-60 min, 4 ºC) to remove any precipitate that developed during storage. We used an extinction coefficient of 19,060 $M^{-1} cm^{-1}$ at $\lambda = 280$ nm to measure the concentration of profilin.

Supplemental References

Fan, J., Saunders, M.G., and Voth, G.A. (2012). Coarse-Graining Provides Insights on the Essential Nature of Heterogeneity in Actin Filaments. Biophys J *103*, 1334-1342.

Goujon, M., McWilliam, H., Li, W., Valentin, F., Squizzato, S., Paern, J., and Lopez, R. (2010). A new bioinformatics analysis tools framework at EMBL-EBI. Nucleic acids research *38*, W695-699.

Kaiser, D.A., Goldschmidt-Clermont, P.J., Levine, B.A., and Pollard, T.D. (1989). Characterization of renatured profilin purified by urea elution from poly-L-proline agarose columns. Cell Motil Cytoskel *14*, 251-262.

Larkin, M.A., Blackshields, G., Brown, N.P., Chenna, R., McGettigan, P.A., McWilliam, H., Valentin, F., Wallace, I.M., Wilm, A., Lopez, R.*, et al.* (2007). Clustal W and Clustal X version 2.0. Bioinformatics *23*, 2947-2948.

Lu, J., and Pollard, T.D. (2001). Profilin binding to poly-L-proline and actin monomers along with ability to catalyze actin nucleotide exchange is required for viability of fission yeast. Mol Biol Cell *12*, 1161-1175.

MacLean-Fletcher, S., and Pollard, T.D. (1980). Identification of a factor in conventional muscle actin preparations which inhibits actin filament self-association. Biochem Biophys Res Commun *96*, 18-27.

Sali, A., and Blundell, T.L. (1993). Comparative Protein Modeling by Satisfaction of Spatial Restraints. J Mol Biol *234*, 779-815.